Research Article

Core-shell Fe₃O₄/SiO₂/TiO₂ Magnetic Modified Ag for the Photocatalytic Degradation of Congo Red Dye and Antibacterial Activity

Poedji Loekitowati Hariani[1],*, S. Salni[2], Muhammad Said[1], Rahfi Farahdiba[1]

[1]Research Group on Magnetic Materials, Department of Chemistry, Faculty of Mathematics and Natural Sciences, Universitas Sriwijaya, Ogan Ilir 30662, Indonesia.
[2]Department of Biology, Faculty of Mathematics and Natural Sciences, Universitas Sriwijaya, Ogan Ilir 30662, Indonesia.

Abstract

Disposal of dye wastewater can induce detrimental consequences for human health and the environment. The study aims to synthesize composites consisting of core-shell Fe₃O₄/SiO₂/TiO₂ modified with Ag. The composites comprise a Fe₃O₄ core, a SiO₂ interlayer, and a TiO₂ shell, with Ag being mobilized on the surface of the core and shell structures. Fe₃O₄/SiO₂/TiO₂@Ag composite was employed in the photocatalytic degradation of Congo red dye and antibacterial activity test. The degradation was facilitated by visible light irradiation while considering different factors such as pH solution, the photocatalyst dosage, and the dye's initial concentration. The composite was characterized using X-ray Diffraction (XRD), Fourier Transform Infrared (FTIR), Scanning Electron Microscopy-Electron Dispersive X-ray Spectroscopy (SEM-EDS), Vibrating Sample Magnetometer (VSM), and UV-Vis Diffuse Reflectance Spectroscopy (UV-Vis DRS). The findings indicated that the composite exhibited strong magnetic, measuring 49.4 emu/g, with a band gap of 2.92 eV. The composite showed commendable catalytic properties, with degradation efficiency of 96.52% for Congo red dye under conditions: a pH solution of 4, a dosage of 0.5 g/L, and a dye concentration of 10 mg/L at 100 min of irradiation. The photocatalytic degradation kinetic is align with pseudo-first-order reactions. The composite also exhibits remarkable stability and efficiency with 4.83% decline in degradation efficiency after five cycles. Fe₃O₄/SiO₂/TiO₂@Ag composite exhibited antibacterial activity against *Escherichia coli* and *Staphylococcus aureus* with a Minimum Inhibitory Concentration (MIC) value of 250 µg/L.

Keywords: Core-shell; Fe₃O₄/SiO₂/TiO₂@Ag; photocatalytic degradation; Congo red dye; antibacterial

1. Introduction

The improper management of synthetic dyes derived from diverse industries, including textiles, food, paper, plastics, medicines, and cosmetics, poses a significant environmental concern due to its potential risks to human health and the ecosystem [1–3]. Approximately 10-15% of the dye is rendered unusable after its application in the coloring [4]. The composition comprises hazardous constituents, including heavy metal ions and aromatic compounds [5]. At lower concentrations, they have been observed to induce adverse effects on aquatic organisms [6]. Several studies have indicated that reactive dyes, even in exceedingly low concentrations (<1 mg/L), change the appearance and clarity of the waters. Furthermore, many dyes and their

---

* Corresponding Author.
  Email: puji_lukitowati@mipa.unsri.ac.id (P.L. Hariani)

breakdown can potentially result in significant health complications [7,8]. Dyes can potentially impede photosynthesis, disrupt the ecosystem's equilibrium, possess toxicity, and exhibit mutagenic properties [9,10]. Congo red is one of the dyes frequently employed and identified as an anionic dye, possessing the molecular formula $C_{32}H_{22}N_6Na_2O_6S_2$. The dye falls under the classification of azo dyes, characterized by the presence of the azo group ($-N=N-$) [5]. Congo red dye possesses an intricate molecular arrangement and multiple functional groups, presenting challenges in its natural degradation [11].

Therefore, various techniques have been employed to eliminate Congo red dyes, such as adsorption [12], photocatalytic degradation [13], sonoelectrochemical degradation [14], oxidation and biotertiary treatment [15], and electrocoagulation [16]. Advanced oxidation processes (AOPs) is an effective and efficient method for wastewater, either through complete mineralization or transformation into a less toxic alternative [17]. The utilization of AOPs that rely on photocatalysis is founded upon the action of highly reactive radicals, specifically hydroxyl radicals. These radicals effectively oxidize organic compounds, transforming them into innocuous byproducts, CO_2 and H_2O [18,19]. The approach is widely regarded as significantly more effective than other methodologies due to its efficacy, fast degradation rate, non-selectivity in contaminant oxidation, and economical nature [17,20].

TiO_2 is a highly prevalent catalyst utilized extensively in waste treatment. It exhibits a notable degree of photocatalytic efficiency, demonstrating its ability to initiate and facilitate chemical reactions under light exposure. Additionally, It possesses the advantages of being non-toxic, chemically stable, and cost-effective [21]. TiO_2 and its composites have been widely employed in various photocatalytic processes. For instance, TiO_2 nanotubes have been utilized to degrade Rhodamine B [22]. TiO_2/GO composites have also removed oxytetracycline and Congo red [21] and $CoFe_2O_4/SiO_2/TiO_2$ has been used to degrade 2,4-dinitrotoluene [23]. The primary impediment to utilizing TiO_2 in the photocatalytic process is effectively separating and retrieving TiO_2 when it is in a solution. TiO_2 has been observed to be readily released and subsequently lost in solution, resulting in secondary pollution [24,25]. Furthermore, it should be noted that TiO_2 possesses a large bandgap with a value of 3.2 eV that restricts its ability to absorb energy solely to the ultraviolet region [26]. Therefore, a ferrites compound as a core is needed, namely Fe_3O_4, $CoFe_2O_4$, and $ZnFe_2O_4$ [27]. Fe_3O_4, exhibits commendable stability and remarkable magnetic properties [28]. The magnetic properties enable the facile and expeditious separation of the photocatalyst and solution utilizing an external magnet.

To prevent interactions between Fe_3O_4 and TiO_2, it is necessary to introduce a layer of SiO_2 to prevent the electron-hole recombination process [29]. In addition, the layer also hinders the dissolution of Fe_3O_4 into the solution and mitigates the impact of photodissolution [30,31]. SiO_2 additionally serves as a protective barrier for Fe_3O_4, preventing its clumping together and shielding it from oxidation reactions [32]. SiO_2 is optimal as a coating due to its inherent thermal and chemical stability [33]. For example, $ZnFe_2O_4/SiO_2/TiO_2$ has been utilized for the photocatalytic degradation of etodolac [34]. Similarly, $Fe_3O_4@SiO_2@CeO_2$ has been employed to degrade Methylene blue dye [35]. In another case, $NiFe_2O_4/SiO_2/NiO$ has been utilized for the photocatalytic degradation of Methylene blue [36].

Aside from the chemical risk, wastewater frequently possesses pathogenic bacteria, namely *Escherichia coli* (*E. coli*) and *Staphylococcus aureus* (*S. aureus*). Metals and metal oxides have been identified as potential contenders for the process of photocatalytic degradation as well as for their possible use in antibacterial applications [37,38]. The dispersion of Ag on the surface of TiO_2 has been found to enhance the antibacterial activity against *S. epidermidis*, *S. aureus*, and *E. coli* [39]. Ag possesses antibacterial properties that effectively eliminate a wide range of bacteria commonly encountered daily, even those that have developed antibiotic resistance [40]. The interaction between Ag and cell membranes leads to the disruption of system metabolism [41]. Additionally, Ag exhibits light absorption properties that extend into the visible region. The presence of Ag can cause the narrowing of the band gap. The presence of Ag can cause the narrowing of the band gap. Ag acts as a reservoir of electrons and traps photogenerated electrons, thereby reducing the recombination process [42,43].

The synthesis of a magnetic core-shell structure $Fe_3O_4/SiO_2/TiO_2@Ag$ was conducted in this study. The characterization of the product was performed utilizing various analytical techniques, namely X-ray diffraction (XRD), Fourier-transform infrared spectroscopy (FTIR), scanning electron microscopy with energy-dispersive X-ray spectroscopy (SEM-EDS), vibrating sample magnetometry (VSM), ultravio-

let-visible diffuse reflectance spectroscopy (UV-Vis DRS). The product was employed in the photocatalytic degradation of the Congo red dye. Lastly, an agar diffusion method was utilized to evaluate the antibacterial efficacy against *E. coli* and *S. aureus* bacterial strains.

2. Materials and Methods

2.1 Material

Commercial chemicals consist of $FeCl_3.6H_2O$ ($\geq 99\%$), $FeCl_2.4H_2O$ ($\geq 99\%$), tetraethyl orthosilicate (TEOS) ($\geq 98\%$), NH_4OH ($\geq 33\%$),, NaOH ($\geq 99.9\%$), ethanol ($\geq 96\%$), titanium tetrabutoxide (TBOT) ($\geq 97\%$), $AgNO_3$ ($\geq 99.5\%$), $NaBH_4$ ($\geq 98\%$) from Merck, Germany, and Congo red dye ($\geq 75\%$), from Sigma Aldrich.

2.2 Synthesis of Fe_3O_4

Synthesis of Fe_3O_4 using the coprecipitation method. As much as 5.41 g of $FeCl_3.6H_2O$ and 1.99 g of $FeCl_2.4H_2O$ will be dissolved in 50 mL of deionized water. The mixture was stirred for 30 min at 60 °C while flowing with nitrogen gas. 1 M NaOH solution was added to the mix gradually until a black precipitate formed and the pH was ± 11. The precipitate obtained was washed with distilled water and ethanol until the pH was neutral. The precipitate is separated from the solution using an external magnet and dried under vacuum at 60 °C.

2.3 Synthesis of Fe_3O_4/SiO_2

The Stober method, adapted from Romdoni *et al.* [44], for synthesized Fe_3O_4/SiO_2. As much as 0.1 g of Fe_3O_4 were dissolved in a solution consisting of 40 mL of ethanol, 10 mL of distilled water, and 1.2 mL of ammonia solution (25%) through the sonification process for approximately one hour. Then, a total of 20 mL of solution made from 2 mL of TEOS diluted in 20 mL of ethanol is slowly added. The process of sonication was then sustained for approximately one hour. The precipitate was separated from the solution by employing an external magnet. Subsequently, the precipitate was subjected to a thorough washing process involving distilled water and ethanol. Finally, the precipitate was dried under vacuum conditions at a temperature of 60 °C.

2.4 Synthesis of $Fe_3O_4/SiO_2/TiO_2$

The synthesis of $Fe_3O_4/SiO_2/TiO_2$ by dissolving 0.15 g of Fe_3O_4/SiO_2 in 50 mL of ethanol. Then, sonication was performed for approxi-mately 30 min. A gradual addition of up to 2 mL of titanium tetrabutoxide (TBOT) was performed while sonication was maintained for 20 min. A volume of 1 mL of ammonia solution (25%) was introduced into the mixture. Subsequently, agitation was conducted at 70 °C for 4 h. The product is isolated from the solution using an external magnet and subsequently subjected to washing procedures involving distilled water and ethanol. The product underwent calcination at 350 °C for 2 h.

2.5 Synthesis of $Fe_3O_4/SiO_2/TiO_2@Ag$

The method employed for impregnating Ag on $Fe_3O_4/SiO_2/TiO_2$ was conducted according to Yildiz *et al.* [45], with a modification involving the reduction of $AgNO_3$ using $NaBH_4$. A solution containing 0.15 g of $Fe_3O_4/SiO_2/TiO_2$ was prepared by dissolving it in 30 mL of distilled water, followed by sonication for 15 min. Then, a solution of $AgNO_3$ 0.2 M was introduced, and the sonification process was sustained for 2 h. Subsequently, a solution containing 0.6 g of $NaBH_4$ was introduced, and agitation was conducted employing a magnetic stirrer for 2 h. The product is isolated from the solution with an external magnet, subsequently subjected to washing with distilled water and ethanol, and ultimately dried under vacuum conditions at a temperature of 60 °C.

2.6 Characterizations

XRD analysis was conducted on Fe_3O_4, Fe_3O_4/SiO_2, $Fe_3O_4/SiO_2/TiO_2$, and $Fe_3O_4/SiO_2/TiO_2@Ag$ using the XRD XPERT PRO PANAlytical instrument with Cu-Kα radiation (λ = 0.15418 Å, 40 kV, and 40 mA) within the angular range of 10 to 90°. The determination of the morphology and composition of the elements was conducted through the SEM-EDS (JSM 6510 LA) instrument. The identification of functional groups was accomplished through FTIR spectroscopy, employing the Thermo scientific Nicolet iS-10 instrument. The samples were prepared using KBr pellets and analyzed within the wave number range of 400–4000 cm^{-1}. The magnetic characteristics of the substance were assessed using a Vibration Sample Magnetometer (VSM Oxford Type 1.2 H). The optical band gap value of the sample was determined through the application of UV-Vis DRS analysis utilizing the Orion Aquamate 8000 instrument.

2.7 Photocatalytic Activity

The photocatalytic degradation of Congo red dye was performed multiple times under differ-

ent experimental conditions, including varying pH levels (ranging from 2 to 8), different dosages of Fe₃O₄/SiO₂/TiO₂@Ag (0.15, 0.5, 0.75, and 1.0 g/L), and initial concentrations of Congo red dye (10, 20, 30, and 40 mg/L). The setup involved a 125-watt mercury lamp as the irradiation source, positioned at a distance of 15 cm from the solution. The solution, mixed with the composite, was subjected to a pre-irradiation process by placing it in a reactor under stirring conditions without light to attain adsorption equilibrium. Subsequently, the solution was irradiated for 0-120 min, with intervals of 20 min. After photocatalytic degradation, the absorbance of the dye solution was measured with the Type Orion Aquamate 8000 UV-Vis spectrophotometer. Total organic carbon (TOC) was measured using a Total Organic Carbon Analyzer (Shimadzu UV 3600).

The recyclability process was evaluated by subjecting composites to five cycles of photocatalytic degradation. The Fe₃O₄/SiO₂/TiO₂@Ag composite, following its utilization in the process of photocatalytic degradation of Congo red dye, underwent a subsequent purification step involving rinsing with distilled water and subsequent drying at a temperature of 60 °C for 3 h.

2.8 Antibacterial Activity of Fe₃O₄/SiO₂/TiO₂@Ag

The antibacterial efficacy of Fe₃O₄/SiO₂/TiO₂@Ag was evaluated using the agar diffusion method against *E. coli* and *S. aureus* bacteria. The concentrations of Fe₃O₄/SiO₂/TiO₂@Ag exhibited variation, specifically at 2000, 1000, 500, 250, 125, and 62.5

µg/mL, employing DMSO as the solvent. The Fe₃O₄/SiO₂/TiO₂@Ag solution underwent homogenization through an ultrasonic probe. A sterile sampler transferred 3 µL of each suspension onto 6.0 mm paper discs. The bacterial strains were obtained from a recently cultured bacterial suspension with a density of 0.5 McFarland. These strains were subsequently cultured individually on Mueller-Hinton agar plates. Later, the disk is carefully transferred onto the agar plate using aseptic forceps. The dish was then incubated at 37 °C for 24 h. Lastly, the measurement of the inhibition zone's diameter was conducted.

3. Results and Discussion

3.1 Characterization of Fe₃O₄, Fe₃O₄/SiO₂, Fe₃O₄/SiO₂/TiO₂ and Fe₃O₄/SiO₂/TiO₂@Ag

The XRD patterns of Fe₃O₄, Fe₃O₄/SiO₂, Fe₃O₄/SiO₂/TiO₂, and Fe₃O₄/SiO₂/TiO₂@Ag are shown in Figure 1. The 2θ measured are 30.30°, 35.51°, 43.44°, 54.31°, 57.33°, and 63.21°, which correspond to crystal plane index (220), (331), (400), (422), (511) and (440) of Fe₃O₄ database according to the JCPDS card No. 75-0449 with inverse-spinel structure. The Fe₃O₄/SiO₂ exhibits a peak similar to that of Fe₃O₄, albeit with reduced intensity. The absence of diffraction peaks for SiO₂ suggests that the SiO₂ layer is amorphous [41,46]. The detection of TiO₂ in the Fe₃O₄/SiO₂/TiO₂ peak was at 2θ of 25.07° (101) and 48.09° (200), indicating of anatase phase (JCPDS cards No. 21-1272). The measurements of the 2θ at 38.68° (111), 44.21° (200) and 77.37° (311) provide evidence that the distribution of Ag on the surface of the Fe₃O₄/SiO₂/TiO₂ adheres to the face-
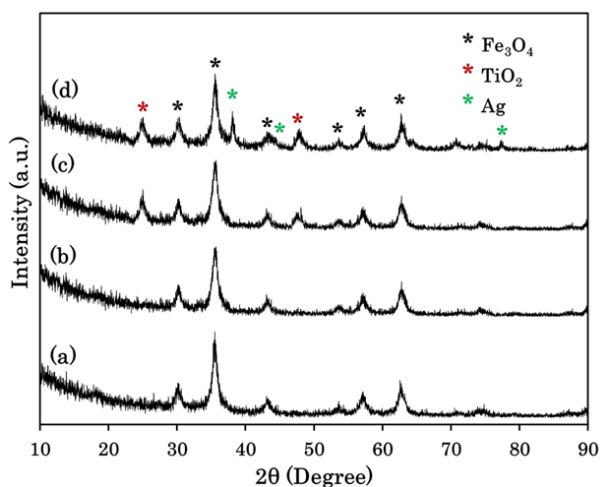
Figure 1. XRD pattern of (a) Fe₃O₄, (b) Fe₃O₄/SiO₂, (c) Fe₃O₄/SiO₂/TiO₂ and (d) Fe₃O₄/SiO₂/TiO₂@Ag.
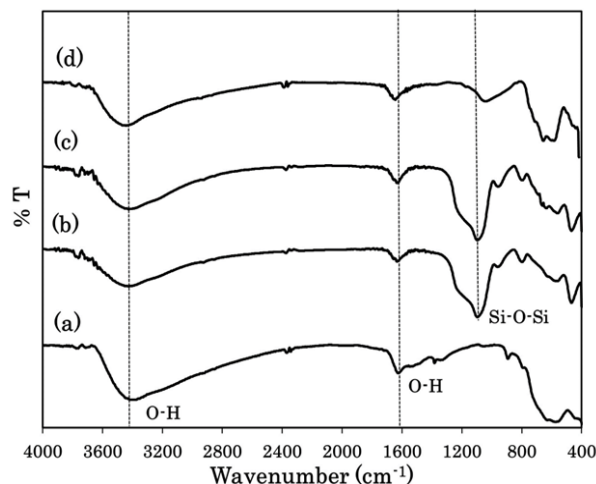
Figure 2. FTIR spectra of (a) Fe₃O₄, (b) Fe₃O₄/SiO₂, (c) Fe₃O₄/SiO₂/TiO₂ and (d) Fe₃O₄/SiO₂/TiO₂@Ag.

centered cubic structure (JCPDS cards No. 03-092). The average crystallite size was determined using the Debye-Scherrer equation, it was found that the crystal sizes of Fe_3O_4, Fe_3O_4/SiO_2, $Fe_3O_4/SiO_2/TiO_2$ and $Fe_3O_4/SiO_2/TiO_2@Ag$ were 25, 23, 19 and 19 nm. The presence of SiO_2 inhibits crystal

growth. Other research shows that SiO_2 doping on $NiFe_2O_4$ also reduces crystal size [47].

Figure 2 displays the FTIR spectra of Fe_3O_4, Fe_3O_4/SiO_2, $Fe_3O_4/SiO_2/TiO_2$, and $Fe_3O_4/SiO_2/TiO_2@Ag$. The spectral peaks seen at wave numbers between 1620–1630 cm^{-1} and 3398–3421 cm^{-1} are evidence of H−O−H vibra-
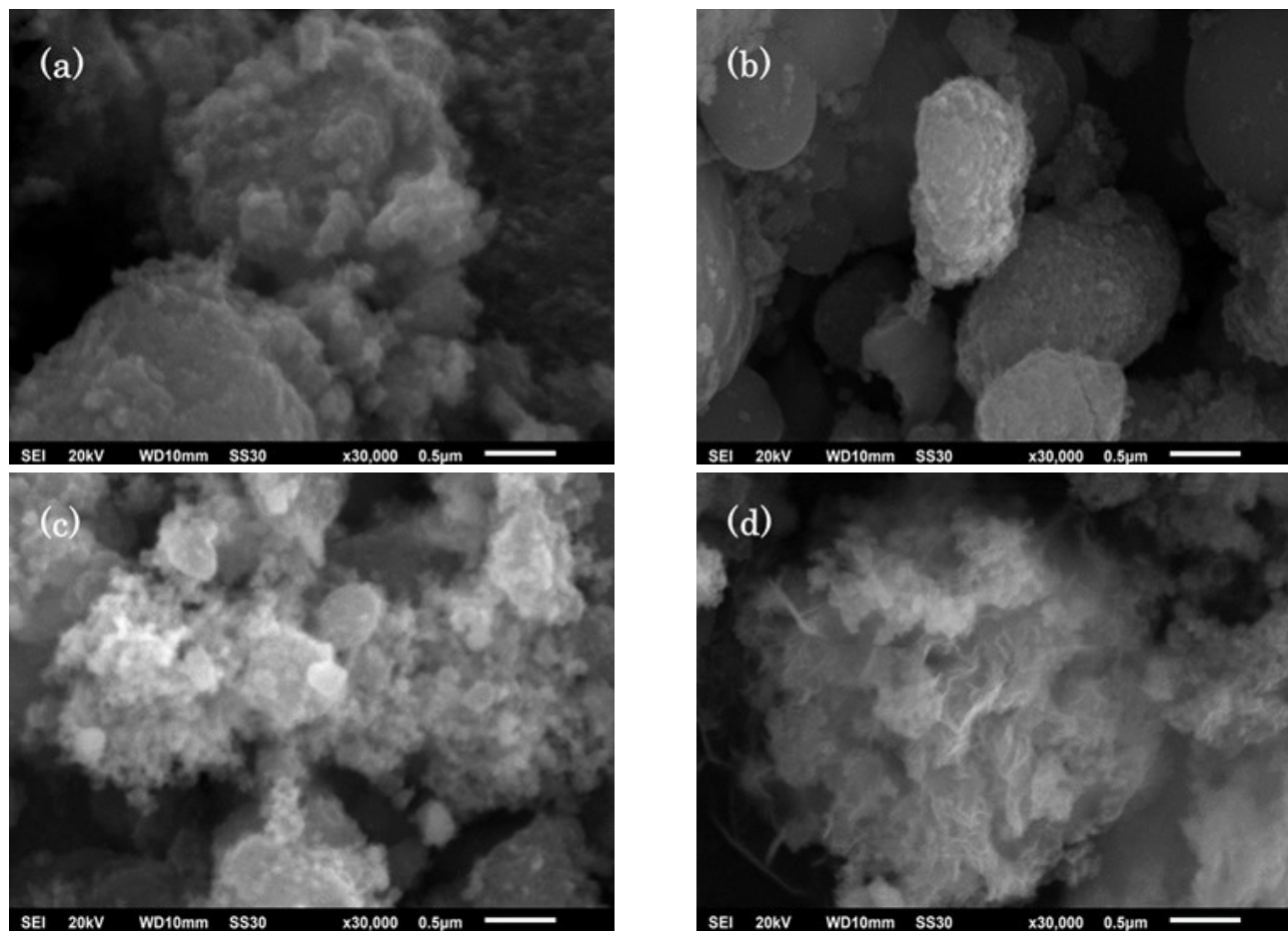
Figure 3. Morphology of (a) Fe_3O_4, (b) Fe_3O_4/SiO_2, (c) $Fe_3O_4/SiO_2/TiO_2$ and (d) $Fe_3O_4/SiO_2/TiO_2@Ag$.
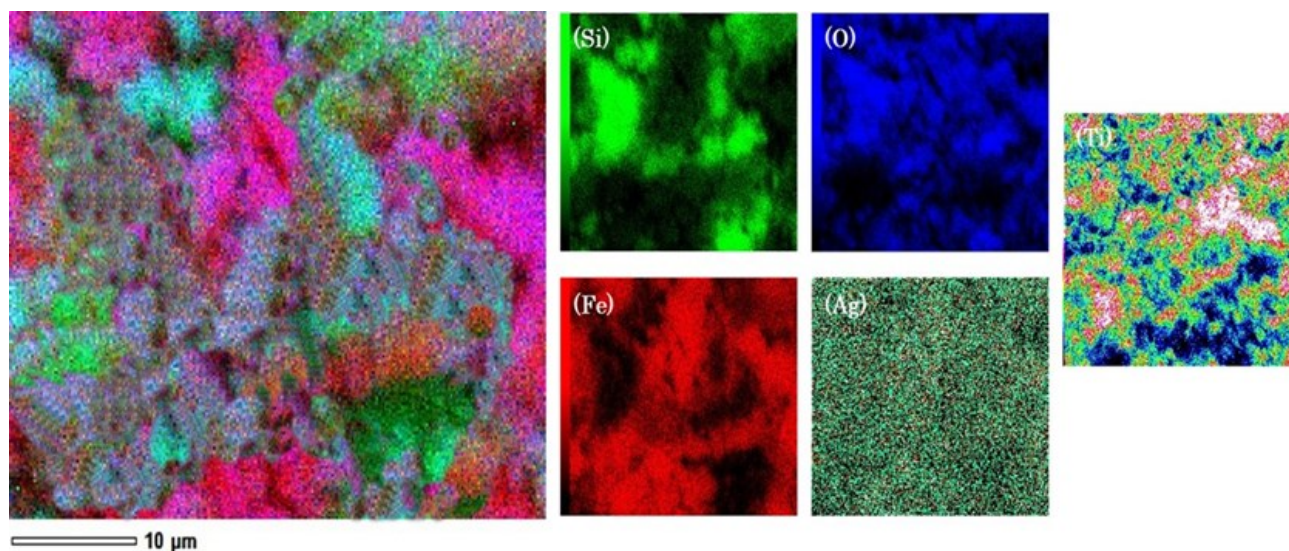

Figure 4. Elemental mapping of $Fe_3O_4/SiO_2/TiO_2@Ag$.

tions and the bending vibrations of water molecules [48]. The peaks within the 1080–1100 cm^{-1} range indicate stretching and deformation vibrations associated with the Si−O−Si bond [49]. The aforementioned peak is observed in the materials Fe_3O_4/SiO_2, $Fe_3O_4/SiO_2/TiO_2$, and $Fe_3O_4/SiO_2/TiO_2@Ag$, with corresponding wave numbers of 1091.70, 1081.25, and 1080.49 cm^{-1}. The spectra of Fe_3O_4/SiO_2 and $Fe_3O_4/SiO_2/TiO_2$ exhibit distinct peaks at wave numbers 459.05 and 455.26 cm^{-1}, corresponding to the asymmetric stretching of Si−O−Si bonds. However, in the case of $Fe_3O_4/SiO_2/TiO_2@Ag$, these peaks are observed with reduced intensity. The vibrational mode corresponding to the Fe−O−Fe bond in Fe_3O_4 is characterized by a peak at wave numbers ranging from 570 to 630 cm^{-1} [50]. The peak overlaps with the Ti−O and Ti−O−Ti vibrations, observed within the wave number range of 500–700 cm^{-1} [48]. The FTIR spectra of $Fe_3O_4/SiO_2/TiO_2@Ag$ did not exhibit a discernible shift in wavenumber compared to those of $Fe_3O_4/SiO_2/TiO_2$. However, there was a noticeable alteration in the intensity of the spectra. This phenomenon can be attributed to the lack of infrared light absorption by Ag [49].

Figure 3 depicts the morphological characteristics of Fe_3O_4, Fe_3O_4/SiO_2, $Fe_3O_4/SiO_2/TiO_2$, and $Fe_3O_4/SiO_2/TiO_2@Ag$. Meanwhile, Figure 4
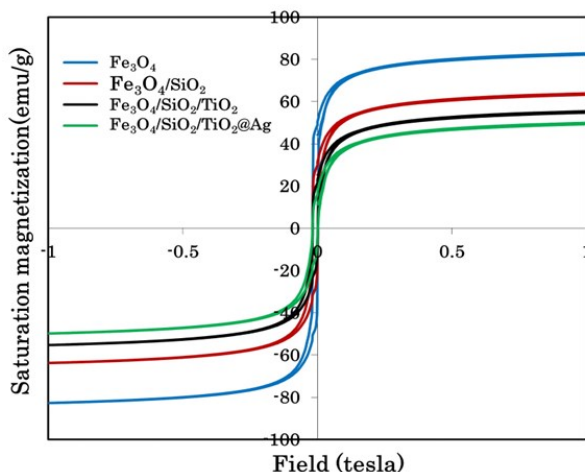
provides an elemental mapping analysis for $Fe_3O_4/SiO_2/TiO_2@Ag$. The morphology of Fe_3O_4 exhibits an irregular structure characterized by agglomeration. In contrast, Fe_3O_4/SiO_2 displays a spherical morphology, suggesting the presence of a coating on the Fe_3O_4 surface. The $Fe_3O_4/SiO_2/TiO_2$ and $Fe_3O_4/SiO_2/TiO_2@Ag$ surfaces exhibit analogous characteristics, specifically a flake-like morphology encompassed by spherical particles. Based on mapping analysis, it can be concluded that the surface of $Fe_3O_4/SiO_2/TiO_2$ at Ag exhibited a lack of homogeneity. Certain locations exhibited a prevalence of Fe and Si, whereas the composite surface displayed a distribution of Ag.

The composition of the elements derived from the EDS analysis is presented in Table 1. The compound Fe_3O_4 consists of Fe and O. When SiO_2 is introduced, the proportion of Fe in the compound decreases. The core material utilized in this context is Fe_3O_4, whereas SiO_2 serves the purpose of coating the Fe_3O_4. The observed reduction in the proportion of Fe and the emergence of Si elements provide evidence of the effective encapsulation of Fe_3O_4 with SiO_2. Similarly, the successful synthesis of $Fe_3O_4/SiO_2/TiO_2@Ag$ can be inferred from the presence of Ti and Ag elements.

According to Figure 5, it can be observed that the saturation magnetization value follows: $Fe_3O_4 > Fe_3O_4/SiO_2 > Fe_3O_4/SiO_2/TiO_2 > Fe_3O_4/SiO_2/TiO_2@Ag$. The saturation magnetization values of the respective samples are 82.3, 63.3, 54.8, and 49.4 emu/g. The saturation magnetization values of Fe_3O_4 obtained in this study were higher than those reported in previous studies. The values were found to be 50.7 emu/g [41], 55.25 emu/g [44] and 63.6 emu/g [51]. The formation of the core-shell leads to a reduction in magnetic properties since the SiO_2 coating, being non-magnetic, hinders the propagation of the magnetic field. Similar findings have been observed in other studies, indicating that the saturation magnetization value of Fe_3O_4 is higher than Fe_3O_4/SiO_2 and $Fe_3O_4/SiO_2/NiO$ [36].

The optical properties of $Fe_3O_4/SiO_2/TiO_2@Ag$ were examined using DRS

Figure 5. Magnetic properties of Fe_3O_4, Fe_3O_4/SiO_2, $Fe_3O_4/SiO_2/TiO_2$ and $Fe_3O_4/SiO_2/TiO_2@Ag$.

Table 1. Elemental composition of Fe_3O_4, Fe_3O_4/SiO_2, $Fe_3O_4/SiO_2/TiO_2$ and $Fe_3O_4/SiO_2/TiO_2@Ag$ from EDS analysis.

Materials	Fe (%)	O (%)	Si (%)	Ti (%)	Ag (%)
Fe_3O_4	71.48	28.52	-	-	-
Fe_3O_4/SiO_2	37.96	43.64	18.40	-	-
$Fe_3O_4/SiO_2/TiO_2$	24.78	46.32	16.56	12.34	-
$Fe_3O_4/SiO_2/TiO_2@Ag$	21.50	43.25	15.42	11.49	8.34

UV-Vis spectroscopy to determine the band gap (E_g). In this research, a comparison was made between the band gap values of the material under investigation and commercially available TiO$_2$. The determination of the band gap value is achieved through the utilization of the Tauc equation in the following manner:

$$\left(\alpha h v\right)^n = B\left(h v - E_g\right) \qquad (1)$$

E_g denotes the optical band gap, α symbolizes the absorption coefficient, h corresponds to Planck's constant, v signifies the frequency of the incident radiation, and n represents a constant that relies on the specific electronic transition being considered (for indirect transition, $n = 2$, while for direct transition, $n = 1/2$). The band gap values of the Fe$_3$O$_4$/SiO$_2$/TiO$_2$@Ag were determined by analyzing the graph of $(\alpha h v)^2$ vs. $h v$. TiO$_2$ is classified as an indirect transition [52]. The data presented in Figure 6(a) demonstrates that Fe$_3$O$_4$/SiO$_2$/TiO$_2$@Ag exhibits a broad absorption peak in the visible region, specifically at wavelengths greater than 400 nm. In contrast, TiO$_2$ displays a distinct absorption peak at a wavelength of 353 nm, which falls within UV region. In Figure 6(b), the band gap value of Fe$_3$O$_4$/SiO$_2$/TiO$_2$@Ag is depicted as 2.92 eV, which is comparatively lower than TiO$_2$ measured at 3.24 eV. The findings suggest that photocatalytic degradation is better suited for use in the region of visible light irradiation. An additional investigation demonstrated that the band gap measurement of TiO$_2$ was determined to be 3.25 eV. However, when incorporating ferrite compounds, NiFe$_2$O$_4$, at concentrations of 4%, 8%, and 12%, the band gap value decreased to 3.19 eV, 3.01 eV, and 2.94 eV, respectively [53].

3.2 Photocatalytic Degradation of Congo red Dye

The photocatalytic degradation of the Congo red dye utilizing the Fe$_3$O$_4$/SiO$_2$/TiO$_2$@Ag composite material is depicted in Figures 7(a)–(d). The quantification of the degraded dye is denoted by C/C_0, which C (mg/L) signifies the concentration of the degradation product, while C_0 (mg/L) represents the initial concentration of the dye. Figure 7(a) shows a plot of initial pH versus ΔpH to obtain pHpzc. The surface material is negative when pHpzc < pH and positively charged when pHpzc > pH [47]. This study obtained the pHpzc Fe$_3$O$_4$/SiO$_2$/TiO$_2$@Ag of 5.77. In Figure 7(b), the impact of pH on the degradation of dye is depicted. The concentration of Congo red dye employed is 20 mg/L in a volume of 50 mL. The dosage utilized is 0.25 mg/L, and the duration of irradiation spans from 0 to 120 min, with intervals of 20 min. The observed decline in the concentration of Congo red dye over a 60 min period was comparatively less pronounced in the absence of irradiation, as evidenced by the graph depicting the 0-60 min interval. This graph exhibited a more gradual slope in the absence of irradiation.

The degradation of Congo red dye at pH 3 and 4 exhibited a nearly equivalent extent, precisely 70.8% and 71.3%, respectively. Notably, an elevation in pH resulted in a reduction in the quantity of dye degradation. Congo red dyes exhibit high solubility in acidic environments, forming sulfonic groups with a negative charge with a pKa of 4.1 (25 °C) [54]. Under conditions of low pH, it can be observed that the composite surface undergoes protonation, resulting in the acquisition of a positive charge (< pHpzc) [55]. Therefore, the electrostatic at-

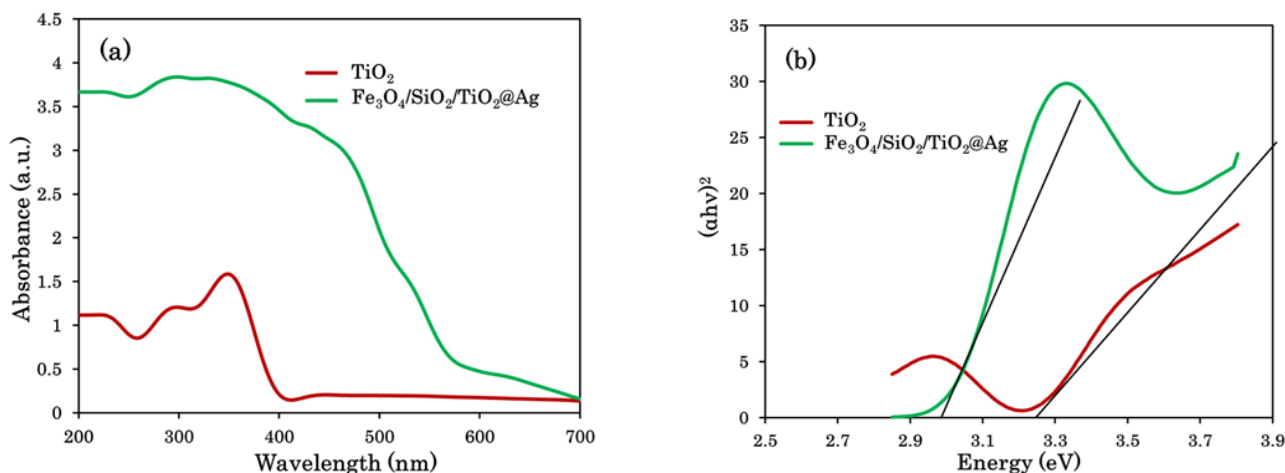Figure 6. Spectra of (a) UV-Vis DRS and (b) Band gap energies of TiO$_2$ and Fe$_3$O$_4$/SiO$_2$/TiO$_2$@Ag.

traction between the dye and the composite material is enhanced. Several research studies have indicated that the most effective conditions for the photocatalytic degradation of Congo red dye involve an acidic pH, such as using $CoFe_2O_4$-TiO_2 at a pH of 3 [56] and C-TiO_2@Fe_3O_4/AC at a pH of 5 [57].

Figure 7(c) shows the highest degradation observed at a dose of 0.50 g/L after 100 min of irradiation, with a degradation percentage of 84.60%. The experiment involved conducting photocatalytic degradation on a solution containing 20 mg/L of Congo red dye in a volume of 50 mL with a pH of 4. Overall, the degradation percentage exhibited an upward trend, starting from a dosage of 0.25 mg/L and reaching its peak at 50 mg/L. Subsequently, the percentage of degradation declined from 0.75 mg/L. The augmentation of composite materials has a detrimental effect on photocatalytic degradation efficiency [56]. When the dose in higher quantities, it increases turbidity, impeding light absorption [5,58].

The impact of varying initial concentrations of Congo red dye (10, 20, 30, and 40 mg/L) on value of C/C_0 is depicted in Figure 7(d). Photo-
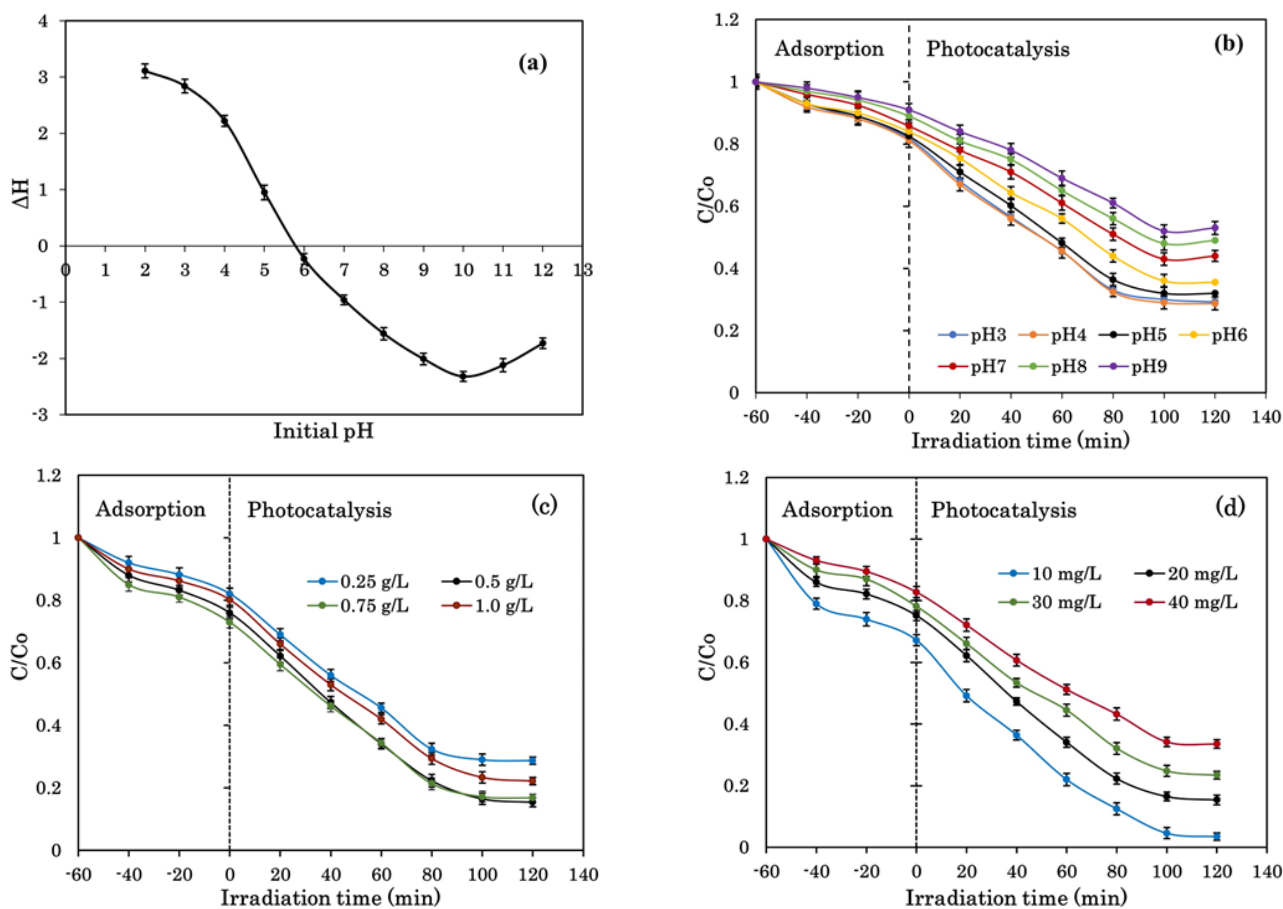
Figure 7. (a) pHpzc and photocatalytic degradation curve of Congo red dye as a function of (b) pH, (c) Catalyst dose, and (d) Initial concentration.

Table 2. Comparison of the photocatalytic degradation of several photocatalysts for the Congo red dye.

Catalyst	pH	Doses (g/L)	Concentration (mg/L)	Time (min)	Removal (%)	Ref.
Co_3O_4/TiO_2/GO	3	0.25	10	90	91	[21]
Fe_2O_3-CeO2	-	2.0	25	180	96	[60]
Fe_2O_3/porous SiO_2	-	1.0	20	180	88	[61]
Ni-TiO_2	2	0.08	80	180	92.31	[62]
$CoFe_2O_4$-TiO_2	3	0.08	10	120	80	[56]
P-ZrO_2 CeO_2 ZnO	-	0.05	10	250	86	[13]
Al-$SrTiO_3$	5	0.02	10	90	81	[63]
Fe_3O_4/SiO_2/TiO_2@Ag	4	0.50	10	100	96.52	In this work

catalytic degradation was conducted under pH 4 and a dosage of 0.5 g/L. The magnitude of degradation of the Congo red dye as a follow 10 mg/L > 20 mg/L > 30 mg/L > 40 mg/L. The greatest photocatalytic degradation observed at the initial concentration 10 mg/L of 96.52%. The efficacy of degradation is influenced by the catalyst's efficiency in absorbing energy. The high initial concentration of the dye hinders light transmission, impeding its absorption by the catalyst. Furthermore, it should be noted that a significant quantity of dye molecules can potentially obstruct the active region of the catalyst surface, resulting in a deficiency in ROS production [59]. Table 2 compares the photocatalytic degradation of the Congo red dye in various research findings. The percentage of photocatalytic degradation utilizing $Fe_3O_4/SiO_2/TiO_2@Ag$ exhibits a higher magnitude in comparison to previous investigations.

The photocatalytic degradation is initiated by the adsorption of Congo red dye onto the catalyst's surface. Moreover, the trigger actively engages in the absorption of radiation, thereby facilitating the process of electron photogeneration from the valence band (VB) to the conduction band (CB), resulting in a positively charged vacancy referred to as a hole (h^+). The photogenerated electron-hole pairs (e^-/h^+) are subsequently captured by the surface of the catalyst [56]. Photogenerated electrons undergo a reaction with O_2 on the surface of the catalyst that leads to ROS, such as $\cdot OH$ and $\cdot O_2^-$ [64,65]. The interaction $\cdot OH$ and $\cdot O_2^-$ with Congo red results in non-toxic inorganic substances and even leads to complete mineralization of the target compound, H_2O and CO_2 [65].

The photocatalytic degradation mechanism is explained as follows: [55]

$$Fe_3O_4/SiO_2/TiO_2@Ag + h\upsilon \rightarrow$$
$$Fe_3O_4/SiO_2/TiO_2@Ag\ (e_{CB}^- + h_{VB}^+) \qquad (2)$$
$$e_{CB}^- + O_2 \rightarrow \cdot O_2^- \qquad (3)$$
$$h_{VB}^+ + H_2O \rightarrow \cdot OH + H^+ \qquad (4)$$
$$Congo\ red\ dye + \cdot OH/\cdot O_2^- \rightarrow$$
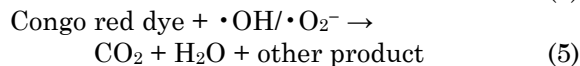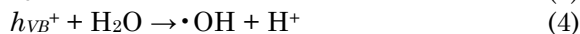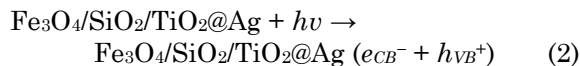$$CO_2 + H_2O + other\ product \qquad (5)$$

Figure 8 represents the effectiveness of removing the Congo red dye through various methods. These methods include photolysis without a catalyst as well as the use of Fe_3O_4, Fe_3O_4/SiO_2, $Fe_3O_4/SiO_2/TiO_2$, and $Fe_3O_4/SiO_2/TiO_2@Ag$, all under the influence of visible light radiation. The initial concentration of the Congo red dye is 10 mg/L with a pH solution of 4, a dose of 0.5 g/L and an irradiation time of 100 min is applied. It is evident that when exposed solely to radiation (photolysis), only a minor fraction of the dye undergoes degradation. The $Fe_3O_4/SiO_2/TiO_2@Ag$ catalyst, when exposed to visible light radiation, exhibits the highest percentage of removal. This observation suggests a synergistic relationship between visible light radiation and the catalyst, resulting in an efficient reduction of the concentration of Congo red dye.

The assessment of mineralization extent necessitates the utilization of total organic carbon (TOC) analysis. The TOC value acquired was determined to be 86.54%. Typically, the TOC value is unable to attain a 100% level. This occurrence signifies that the process of mineralization is incomplete. It implies that not all of the Congo red dye undergoes degradation into
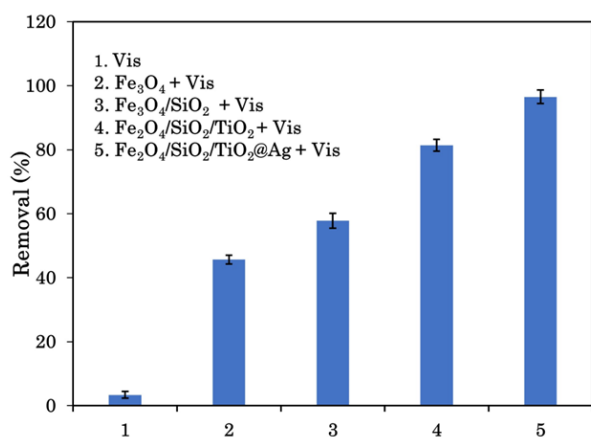
Figure 8. Comparison of removal of Congo red dye using visible irradiation, Fe_3O_4 + Vis, Fe_3O_4/SiO_2 + Vis, $Fe_3O_4/SiO_2/TiO_2$ + Vis and $Fe_3O_4/SiO_2/TiO_2@Ag$ + Vis.

1. Vis
2. Fe_3O_4 + Vis
3. Fe_3O_4/SiO_2 + Vis
4. $Fe_3O_4/SiO_2/TiO_2$ + Vis
5. $Fe_3O_4/SiO_2/TiO_2@Ag$ + Vis
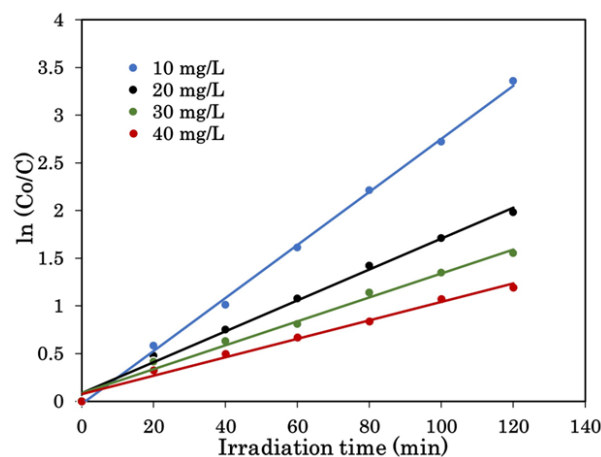
Figure 9. The Congo red dye photocatalytic degradation kinetics using $Fe_3O_4/SiO_2/TiO_2@Ag$ in different concentrations of Congo red dye.

H_2O and CO_2. Instead, some intermediate compounds are formed [66,67]. A research investigation yielded similar findings regarding the TOC value of Congo red dye degradation when utilizing $CoAl_2O_4$-ZnO, which amounted to 66.9% [66]. In another case, the degradation of methyl orange dye was observed to reach 87.6% when employing $NiFe_2O_4/SiO_2/NiO$ [47].

3.3 The Kinetics of Photocatalytic Degradation

The significance of photocatalytic degradation investigations lies in their ability to elucidate the degradation rate of the Congo red dye, thereby providing insights into the duration necessary for the completion of the process. In a broad sense, the pseudo-first-order model is appropriate for the photocatalytic degradation of dyes [68]. It can be exemplified by the utilization of the pseudo-first-order equation by the following [47,69]:

$$-\frac{dC}{dt} = k_{app}C \qquad (6)$$

The integration of these equations becomes:

$$\ln\left(\frac{C_0}{C}\right) = k_{app}t \qquad (7)$$

C_0 and C represents the initial concentration and concentration at each instance (mg/L). Meanwhile, k_{app} symbolizes the pseudo-first-order constant (min^{-1}), and t represents the duration of irradiation (min). The value of k_{app} is determined by calculating the slope of the graph ln C_0/C as a function of time. The data presented in Figure 9 illustrates the kinetics of the photocatalytic degradation process. The experiment used different initial concentrations, precisely 10, 20, 30, and 40 mg/L. The correlation coefficient values (R^2) observed at each concentration were 0.9984, 0.0046, 0.9891, and 0.9875. The observed value is close to 1, suggesting a linear correlation between the quantity of dye that undergoes degradation and time. The observed k_{app} demonstrates an inverse relationship with concentration. As the concentration increases, the value of k_{app} decreases to the following values: 0.0278, 0.0162, 0.0125, and 0.0097 min^{-1}. Additional research studies have also documented a similar case for the photocatalytic degradation of Congo red dye by Al-$SrTiO_3$ at concentrations of 5, 10, and 15, explicitly measuring 0.025, 0.0183, and 0.0109 min^{-1} [63].
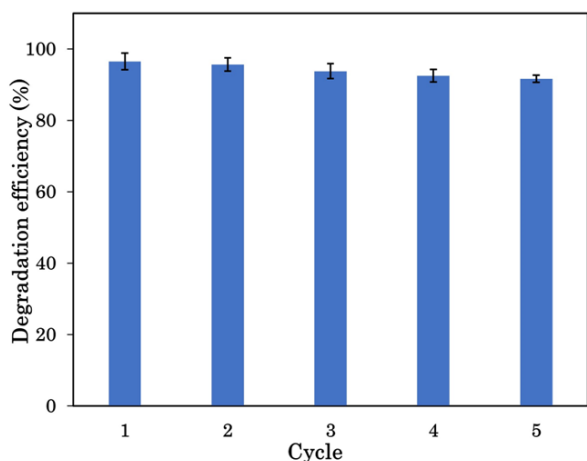

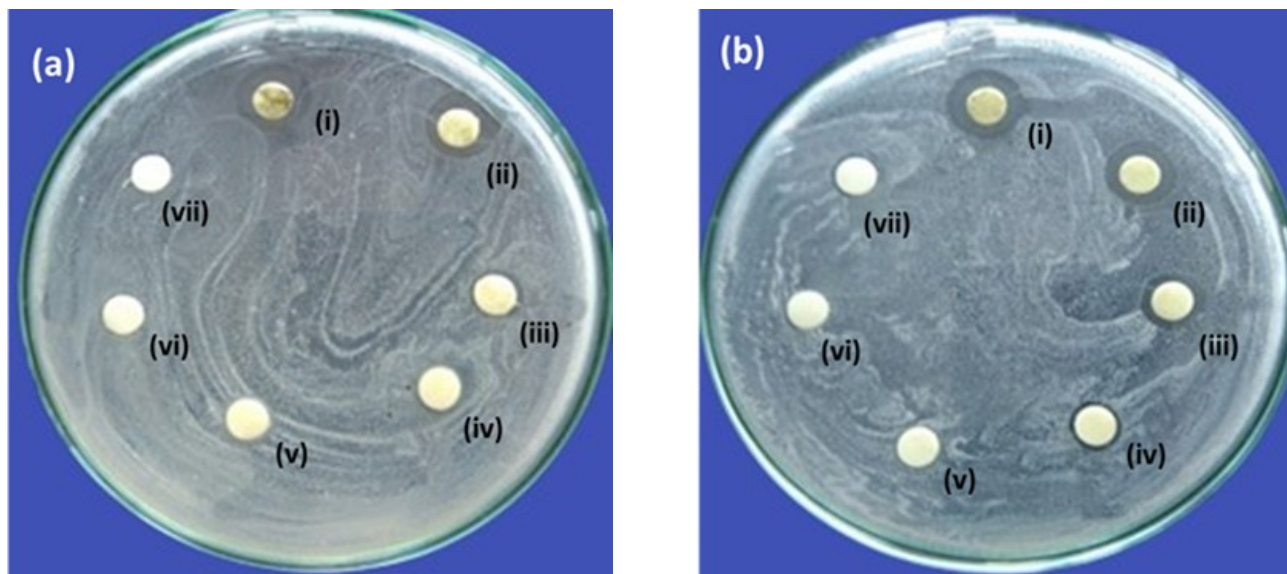Figure 10. Recyclability of $Fe_3O_4/SiO_2/TiO_2$@Ag for photocatalytic degradation of Congo red dye.

Figure 11. Antibacterial activity $Fe_3O_4/SiO_2/TiO_2$@Ag to *E. coli* and *S. aureus*.

3.4 Photocatalyst Recyclability

The assessment of the $Fe_3O_4/SiO_2/TiO_2@Ag$ composite's stability was conducted through an iterative photocatalytic degradation procedure. Figure 10 depicts the degradation efficiency of $Fe_3O_4/SiO_2/TiO_2@Ag$ following five instances of utilization for photocatalytic degradation of Congo red dye. In each iteration, the catalyst is extracted from the solution using an external magnet. Subsequently, it undergoes a thorough cleansing process involving ethanol and water. Finally, it is dried in preparation for the subsequent phase [47,51]. The decline in degradation capability following five cycles amounted to 4.83%. It suggests that the composite material exhibits stability, recyclability, and effectiveness in facilitating the photocatalytic degradation.

3.5 Antibacterial Activity

The antibacterial characteristics of $Fe_3O_4/SiO_2/TiO_2@Ag$ were assessed using the agar diffusion method on *E. coli* and *S. aureus* bacteria. The concentrations utilized for $Fe_3O_4/SiO_2/TiO_2@Ag$ were 2000, 1000, 500, 250, 125, and 62.5 µg/mL, with DMSO serving as the negative control. Figure 11 displays the diameter of the inhibition zone corresponding to each concentration. The bactericidal effect of $Fe_3O_4/SiO_2/TiO_2@Ag$ on both strains is demonstrated by the zone of inhibition, as depicted in Table 3. The concentration of $Fe_3O_4/SiO_2/TiO_2@Ag$ influences the inhibition zone's size. Specifically, as the concentration increases, the diameter of the inhibition zone also increases. According to Ramdoni *et al.* [44], it was observed that the diameter of the inhibition zone for *E. coli* and *S. aureus* exhibited an upward trend as the concentrations of $Fe_3O_4@SiO_2$-Ag increased. The diameter of the inhibition zone ranged from 8 to 11 mm. This investigation revealed that the minimum inhibitory concentration (MIC) at 250 µg/mL and the diameter of the inhibition zone for *E. coli* and *S. aureus* were measured to be 6.70 and 7.38 mm, respectively.

Typically, the antimicrobial efficacy of metals is associated with their capacity to adhere to bacterial cell membranes, engage with macromolecules like DNA and proteins, and generate ROS. These ROS induce the deterioration of cellular structure, ultimately resulting in the demise of the bacterial cells [70]. Furthermore, the presence of Ag nanoparticles leads to the release of ions. This phenomenon is significant as it can potentially enhance the permeability of cellular membranes. The reason behind this lies in the strong affinity and electrostatic attraction that Ag nanoparticles possess towards sulfur-containing proteins [71]. The accumulation of silver ions within the cytoplasm has the potential to induce the denaturation of ribosomes, ultimately resulting in the demise of the cell [72]. Using staining methods, a separate study showed that *E. coli* exposed to $Fe_3O_4SiO_2@MnO_2@Ag$ showed signs of lysis, with stem morphology being changed and damaged as a result [41].

4. Conclusions

Core-shell composites of $Fe_3O_4/SiO_2/TiO_2@Ag$ have been synthesized successfully. The $Fe_3O_4/SiO_2/TiO_2@Ag$ composite possesses superparamagnetic characteristics, which enable the efficient separation of the composite from a solution following its utilization. The composite material exhibits a notable efficiency of 96.52% in the photocatalytic degradation of the Congo red dye. Furthermore, it can be substantiated that the composite material exhibits exceptional stability, thereby enabling its repeated utilization. The $Fe_3O_4/SiO_2/TiO_2@Ag$ composite exhibited remarkable antibacterial efficacy against *E. coli* and *S. aureus*. Based on the aforementioned findings, the composite material possesses a multifaceted function in environmental appli-

Table 3. Inhibition zone of the concentration based on $Fe_3O_4/SiO_2/TiO_2@Ag$.

Code	Concentration (µg/mL)	Inhibition zone (mm)	
		E. coli	*S. aureus*
i	2000	19.10 ± 0.16	21.60 ± 0.08
ii	1000	18.56 ± 0.12	21.05 ± 0.14
iii	500	11.30 ± 0.04	13.15 ± 0.10
iv	250	6.70 ± 0.10	7.38 ± 0.05
v	125	0	0
vi	62.5	0	0
vii	(-)	0	0

cations. Its efficacy extends beyond the mere reduction of dye concentrations, encompassing antibacterial properties as well.

Acknowledgement

CRediT Author Statement

Author contribution: Hariani, P.L: Conceptualization, Investigation, Resources, Experimen, Writing, Salni: Methodology, and Analysis data, Said, M: Review, Editing and Validation; Farahdiba, R: Experiment and analysis data. All authors have read and agreed to the published version of the manuscript.

References

[1] Yan, Y., Yang, H., Yi, Z., Xian, T. (2019). $NaBH_4$-reduction induced evolution of Bi nanoparticles from BiOCl nanoplates and construction of promising Bi@BiOCl hybrid photocatalysts. *Catalysts*, 9(10), 1-20. DOI: 10.3390/catal9100795

[2] Asghar, A., Raman, A.A.A., Daud, W.M.A.W. (2015). Advanced oxidation processes for in-situ production of hydrogen peroxide/hydroxyl radical for textile wastewater treatment: a review. *Journal of Cleaner Production*, 87, 826-838. DOI: 10.1016/j.jclepro.2014.09.010

[3] Pérez-Calderón, J., Santos, M.V., Zaritzky, N. (2020). Synthesis, characterization and application of cross-linked chitosan/oxalic acid hydrogels to improve azo dye (Reactive red 195) adsorption. *Reactive and Functional Polymers*, 155, 1-4. DOI: 10.1016/j.reactfunctpolym.2020.104699

[4] Gómez, V., Larrechi, M.S., Callao, M.P. (2007). Kinetic and adsorption study of acid dye removal using activated carbon. *Chemosphere*, 69(7), 1152-1158. DOI: 10.1016/j.chemosphere.2007.03.076

[5] Malik, A.Q., Mir, T.U.G., Amin, Q., Sathish, M., Kumar, D. (2022). Synthesis, characterization, photocatalytic effect of CuS-ZnO nanocomposite on photodegradation of Congo red and phenol pollutant. *Inorganic Chemistry Communications*, 43, 1-10. DOI: 10.1016/j.inoche.2022.109797

[6] Ahmad, M.A., Rahman, N.K. (2011). Equilibrium, kinetics and thermodynamic of Remazol brilliant orange 3R dye adsorption on coffee husk-based activated carbon. *Chemical Engineering Journal*, 170(1), 154-161. DOI: 10.1016/j.cej.2011.03.045

[7] Lops, C., Ancona, A., Cesare, K.D., Dumontel, B., Garino, N., Canavese, G., Hernandez, S., Cauda, V. (2019). Sonophotocatalytic degradation mechanisms of Rhodamine B dye via radicals generation by micro and nanoparticles of ZnO. *Applied Catalysis B: Environmental*, 243, 629-640. DOI: 10.1016/j.apcatb.2018.10.078

[8] Modirshahla, N., Behnajady, M.A., Rahbarfam, R., Hassani, A. (2012). Effects of operational parameters on decolorization of C. I. Acid red 88 by UV/H_2O_2 process: evaluation of electrical energy consumption. *Clean - Soil, Air, Water,* 40(3), 298-302. DOI: 10.1002/clen.201000574

[9] de Almeida, E.J.R., Mazzeo, D.E.C., Sommaggio, L.R.D., Marin-Morales, M.A., de Andrade, A.R., Corso, C.R. (2019). Azo dyes degradation and mutagenicity evaluation with a combination of microbiological and oxidative discoloration treatments. *Ecotoxicology and Environmental Safety*, 183, 1-10. DOI: 10.1016/j.ecoenv.2019.109484

[10] Huo, J., Yu, D., Li, H., Luo, B., Arulsamy, N. (2019). Mechanistic investigation of photocatalytic degradation of organic dyes by a novel zinc coordination polymer. *RSC Advances*, 9, 39323-39331. DOI: 10.1039/C9RA07821E.

[11] Chakraborty, S., Basak, B., Dutta, S., Bhunia, B., Dey, A. (2013). Decolorization and biodegradation of Congo red dye by a novel white rot fungus *Alternaria alternata* CMERI F6. *Bioresource Technology,* 147, 662-666. DOI: 10.1016/j.biortech.2013.08.117

[12] Harja, M., Buema, G., Bucur, D. (2022). Recent advances in removal of Congo red dye by adsorption using an industrial waste. *Scientific Reports*, 12, 1-18. DOI: 10.1038/s41598-022-10093-3

[13] Hokonya, N., Mahamadi, C., Mukaratirwa-Muchanyereyi, N., Gutu, T., Zvinowanda, C. (2022). Green synthesis of $P − ZrO_2 CeO_2 ZnO$ nanoparticles using leaf extracts of *Flacourtia indica* and their application for the photocatalytic degradation of a model toxic dye, Congo red. *Heliyon*, 8, 1-18. DOI: 10.1016/j.heliyon.2022.e10277

[14] Kalet, S.Z., Ismail, S.A., Ang, W.L., Symes, M.D. (2023). Influence of ultrasound modes on sonoelectrochemical degradation of Congo red and palm oil mill effluent. *Result In Chemistry*, 5, 1-9. DOI: 10.1016/j.rechem.2023.100880

[15] Sathiskumar, K., Alsahi, M.S., Sanganyando, E., Devanesan, S., Arulprakash, A., Rajasekar, A. (2019). Sequential electrochemical oxidation and bio-treatment of the azo dye Congo red and textile effluent. *Journal of Photochemistry and Photobiology B: Biology*, 200, 1-7. DOI: 10.1016/j.jphotobiol.2019.111655

[16] Akhtar, A., Aslam, Z., Asghar, A., Bello, M.M., Raman, A.A.A. (2020). Electrocoagulation of Congo red dye-containing wastewater: Optimization of operational parameters and process mechanism. *Journal of Environmental Chemical Engineering*, 8(5), 1-10. DOI: 10.1016/j.jece.2020.104055

[17] Karim, A.V., Hassani, A., Eghbali, P., Nidheesh, P.V. (2021). Nanostructured modified layered double hydroxides (LDHs)-based catalysts: A review on synthesis, characterization, and applications in water remediation by advanced oxidation processes. *Current Opinion in Solid State and Materials Science*, 26(1), 1-26. DOI: 10.1016/j.cossms.2021.100965

[18] Ge. J., Zhang, Y., Heo, Y.J, Park, S.J. (2019). Advanced design and synthesis of composite photocatalysts for the remediation of wastewater: a review. *Catalysts*, 9(2), 1-32. DOI: 10.3390/catal9020122

[19] Takdastan, A., Kakavandi, B., Azizi, M., Golshan, M. (2018). Efficient activation of peroxymonosulfate by using ferroferric oxide supported on carbon/UV/US system: A new approach into catalytic degradation of bisphenol A. *Chemical Engineering Journal*, 331, 729-743. DOI: 10.1016/j.cej.2017.09.021

[20] Oturan, M.A., Aaron, J.J. (2014). Advanced oxidation processes in water/wastewater treatment: principles and applications. A review. *Critical Reviews in Environmental Science and Technology*, 44 (23), 2577-2641. DOI: 10.1080/10643389.2013.829765

[21] Jo, W., Kumar, S., Isaacs, M.A., Lee, A.F., Karthikeyan, S. (2017). Cobalt promoted TiO$_2$/GO for the photocatalytic degradation of oxytetracycline and Congo red. *Applied Catalysis B: Environmental*, 21, 159-168. DOI: 10.1016/j.apcatb.2016.08.022

[22] Lin, Z., Dong, C., Mu, W., Han, X. (2023). Degradation of Rhodamine B in the photocatalytic reactor containing TiO$_2$ nanotube arrays coupled with nanobubbles. *Advanced Sensor and Energy Materials*, 2(2), 1-7. DOI: 10.1016/j.asems.2023.100054

[23] Sepahvand, S., Bahrami, M., Fallah, N. (2022). Photocatalytic degradation of 2,4-DNT in simulated wastewater by magnetic CoFe$_2$O$_4$/SiO$_2$/TiO$_2$ nanoparticles. *Environmental Science and Pollution Research*, 29, 6479-6490. DOI: 10.1007/s11356-021-13690-3

[24] Shaikh, T., Rathore, A., Kaur, H. (2017). Poly (Lactic Acid) grafting of TiO$_2$ nanoparticles: A shift in dye degradation performance of TiO$_2$ from UV to Solar Light. *Chemistry Select*, 2(23), 6901-6908. DOI: 10.1002/slct.201701560

[25] Yang, C., Dong, W., Cui, G., Zhao, Y., Shi, X., Xia, X., Tang, B., Wang, W. (2017). Enhanced photocatalytic activity of PANI/TiO$_2$ due to their photosensitization-synergetic effect. *Electrochimica Acta*, 247, 486-495. DOI: 10.1016/j.electacta.2017.07.037

[26] Fu, C., Liu, X., Wang, Y., Li, L., Zhang, Z. (2109). Preparation and characterization of Fe$_3$O$_4$@SiO$_2$@TiO$_2$–Co/rGO magnetic visible light photocatalyst for water treatment. *RSC Advances*, 9, 20256-20265. DOI: 10.1039/c9ra04002a

[27] Zielinska-Jurek, A., Bielan, Z., Dudziak, S., Wolak, I., Sobczak, Z., Klimczuk, T., Nowaczyk, G., Hupka, J. (2017). Design and application of magnetic photocatalysts for water treatment. The effect of particle charge on surface functionality. *Catalysts*, 7(12), 360-368. DOI: 10.3390/catal7120360

[28] Liu, X., Ma, Y., Zhang, Q., Zheng, Z., Wang, L., Peng, L. (2018). Facile synthesis of Fe$_3$O$_4$/C composites for broadband microwave absorption properties. *Applied Surface Science*, 445, 82-88. DOI: 10.1016/j.apsusc.2018.03.127

[29] Liu, C., Li, Y., Duan, Q. (2020). Preparation of magnetic and thermal dual-responsive zinc-tetracarboxyl phthalocyanine-g-Fe$_3$O$_4$@SiO$_2$@TiO$_2$-g-poly (N-isopropyl acrylamide) core shell green photocatalyst. *Applied Surface Science*, 503, 1-12. DOI: 10.1016/j.apsusc.2019.144111

[30] Gebrezgiabher, M., Gebreslassie, G., Gebretsadik, T., Yeabyo, G., Elemo, F., Bayeh, Y., Thomas, M., Linert, W. (2019). A C-doped TiO$_2$/Fe$_3$O$_4$ nanocomposite for photocatalytic dye degradation under natural sunlight irradiation. *Journal of Composite Science*, 3(3), 1-11. DOI: 10.3390/jcs3030075

[31] Fan, Y., Ma, C., Li, W., Yin, Y. (2012). Synthesis and properties of Fe$_3$O$_4$/SiO$_2$/TiO$_2$ nanocomposites by hydrothermal synthetic method. *Materials Science in Semiconductor Processing*, 15(5), 582-585. DOI: 10.1016/j.mssp.2012.04.013

[32] Su, J., Zhang, Y., Xu, S., Ding, H., Pan, S., Wang, G., Li, G., Zhao, H. (2014). Highly efficient and recyclable triple-shelled Ag@Fe$_3$O$_4$@SiO$_2$@TiO$_2$ photocatalysts for degradation of organic pollutants and reduction of hexavalent chromium ions. *Nanoscale*, 6, 5181-5192. DOI: 10.1039/C4NR00534A

[33] Gu, J., Zhang, Q., Li, H., Tang, Y., Kong, J., Dang, J. (2007). Study on Preparation of SiO$_2$/Epoxy Resin Hybrid Materials by Means of Sol-Gel. *Polymer-Plastics Technology and Engineering*, 46, 1129-1134. DOI: 10.1080/03602550701558033

[34] Mrotek, E., Dudziak, S., Malinowska, I., Pelczarski, D., Ryzynska, Z., Zielinska-Jurek, A. (2020). Improved degradation of etodolac in the presence of core-shell ZnFe$_2$O$_4$/SiO$_2$/TiO$_2$ magnetic photocatalyst. *Science of The Total Environment*, 724, 1-12. DOI:10.1016/j.scitotenv.2020.138167

[35] Ziaadini, F., Mostafavi, A., Shamspur, T., Fathirad, F. (2019). Photocatalytic degradation of Methylene blue from aqueous solution using Fe$_3$O$_4$@SiO$_2$@CeO$_2$ core-shell magnetic nanostructure as an effective catalyst. *Advances in Environmental Technology*, 2, 127-132. DOI: :10.22104/AET.2020.4137.1204

[36] Hariani P.L. Said M. Salni Rachmat A. Aprianti N. Sthephanie E.A. (2023). Synthesis of Fe$_3$O$_4$/SiO$_2$/NiO magnetic composite: Evaluation of its catalytic activity for Methylene blue degradation. *Global NEST Journal*, 25(2), 36-43. DOI: 10.30955/gnj.004407

[37] Jayaraj, S.K., Sadishkumar, V., Arun, T. Thangadurai, P. (2018). Enhanced photocatalytic activity of V$_2$O$_5$ nanorods for the photodegradation of organic dyes: A detailed understanding of the mechanism and their antibacterial activity, *Materials Science in Semiconductor Processing*, 85, 122-133. DOI: 10.1016/j.mssp.2018.06.00

[38] Rahman, A., Aadil, M., Zulfiqar, S., Alsafari, I.A., Shahid, M., Agboola, P.O., Warsi, M.F., Abdel-Haliem, M.E.F. (2021). Fabrication of binary metal substituted CdO with superior aptitude for dye degradation and antibacterial activity. *Ceramics International*, 47, 8082-8093. DOI: 10.1016/j.ceramint.2020.11.163

[39] Rathnayake, I., Ismail, H., De Silva, C.R., Darsanasiri, N.D., Bose, I. (2015). Antibacterial effect of Ag-doped TiO$_2$ nanoparticles incorporated natural rubber latex foam under visible light conditions. *Iranian Polymer Journal*, 24, 1057-1068. DOI: 10.1007/s13726-015-0393-5

[40] Liong, M., France, B., Bradley, K.A., Zink, J.I. (2009). Antimicrobial activity of silver nanocrystals encapsulated in mesoporous silica nanoparticles. *Advances Materials*, 21(17), 1684-1689. DOI: 10.1002/adma.200802646

[41] Jia, H., Zhang, X., Zeng, X., Cai, R., Wang, Z., Yuan, Y., Yue, T. (2021). Construction of silver nanoparticles anchored flower-like magnetic Fe$_3$O$_4$@SiO$_2$@MnO$_2$ hybrids with antibacterial and wound healing activity. *Applied Surface Science*, 567, 1-11. DOI: 10.1016/j.apsusc.2021.150797

[42] Hassani, A., Faraji, M., Eghbali, P. (2020). Facile fabrication of mpg-C$_3$N$_4$/Ag/ZnO nanowires/Zn photocatalyst plates for photodegradation of dye pollutant. *Journal of Photochemistry & Photobiology A: Chemistry*, 400, 1-15. DOI: 10.1016/j.jphotochem.2020.112665

[43] Ravichandran, K., Sindhuja, E. (2019). Fabrication of cost effective g-C$_3$N$_4$+Ag activated ZnO photocatalyst in thin film form for enhanced visible light responsive dye degradation. *Materials Chemistry and Physics*, 221, 203-215. DOI: 10.1016/j.matchemphys.2018.09.038

[44] Romdoni, Y., Kadja, G.T.M., Kitamoto, Y., Khalil, M. (2023). Synthesis of multifunctional Fe$_3$O$_4$@SiO$_2$-Ag nanocomposite for antibacterial and anticancer drug delivery. *Applied Surface Science*, 610, 1-8. DOI: 10.1016/j.apsusc.2022.155610

[45] Yildiz, A., Bayramol, D.V., Atav, R., Agirgan, A.O., Kurc, M.A., Ergunay, U., Mayer, C., Hadimani, R.L. (2020). Synthesis and characterization of Fe$_3$O$_4$@Cs@Ag nanocomposite and its use in the production of magnetic and antibacterial nanofibrous membranes. *Applied Surface Science*, 521, 1-11, DOI: 10.1016/j.apsusc.2020.146332

[46] Ebrahimzadeh, M.A., Mortazavi-Derazkola, S., Zazouli, M.A. (2019). Eco-friendly green synthesis and characterization of novel Fe$_3$O$_4$/SiO$_2$/Cu$_2$O–Ag nanocomposites using *Crataegus pentagyna* fruit extract for photocatalytic degradation of organic contaminants. *Journal of Materials Science: Materials in Electronics*, 30, 10994-11004. DOI: 10.1007/s10854-019-01440-8.

[47] Hariani, P.L., Said, M., Rachmat, A., Salni, S., Aprianti, N., Amatullah, A.F. (2022). Synthesis of NiFe$_2$O$_4$/SiO$_2$/NiO Magnetic and Application for the Photocatalytic Degradation of Methyl orange dye under UV irradiation. *Bulletin of Chemical Reaction Engineering & Catalysis*, 17(4), 699-711. DOI: 10.9767/bcrec.17.4.15788.699-711

[48] Li, A., Xie, L., Zhou, S., Zhang, M., Ding, Y., Wang, P. (2021). Optimization of Fe$_3$O$_4$/SiO$_2$/N-TiO$_2$/Ag/AgCl core-shell nanomaterial and its properties, repeatability and photocatalytic mechanism. *Journal of Photochemistry and Photobiology A: Chemistry*, 409, 1-11. doi: 10.1016/j.jphotochem.2021.113141

[49] Chi, Y., Yuan, Q., Li, Y., Tu, J., Zhao, L., Li, N., Li, X. (2012). Synthesis of Fe$_3$O$_4$@SiO$_2$–Ag magnetic nanocomposite based on small-sized and highly dispersed silver nanoparticles for catalytic reduction of 4-nitrophenol. *Journal of Colloid and Interface Science*, 383(1), 96-102. DOI: 10.1016/j.jcis.2012.06.027

[50] Shirazi, M., Allafchian, A., Salamati, H. (2023). Design and fabrication of magnetic Fe₃O₄-QSM nanoparticles loaded with ciprofloxacin as a potential antibacterial agent. *International Journal of Biological Macromolecules*, 241, 1-14. DOI: 10.1016/j.ijbiomac.2023.124517

[51] Ammar, S.H., Elaibi, A.I., Mohammed, I.S. (2020). Core/shell Fe₃O₄@Al₂O₃-PMo magnetic nanocatalyst for photocatalytic degradation of organic pollutants in an internal loop airlift reactor. *Journal of Water Process Engineering*, 37, 1-11. DOI: 10.1016/j.jwpe.2020.101240

[52] Boulahbel, H., Benamira, M., Bouremmad, F., Ahmia, N., Kiamouche, S., Lahmar, H., Souici, A., Trari, M. (2023). Enhanced photodegradation of Congo red dye under sunlight irradiation by p-n NiFe₂O₄/TiO₂ heterostructure. *Inorganic Chemistry Communications*, 154, 1-12. DOI: 10.1016/j.inoche.2023.110921

[53] Firtina-Ertis, I., Kerkez-Kuyumcu, O. (2022). Synthesis of NiFe₂O₄/TiO₂-Ag⁺S-scheme photocatalysts by a novel complex-assisted vapor thermal method for photocatalytic hydrogen production. *Journal of Photochemistry & Photobiology, A: Chemistry*, 432, 1-11. DOI: 10.1016/j.jphotochem.2022.114106

[54] Thomas, M., Naikoo, G.A., Sheikh, M.U.D., Bano, M., Khan, F. (2016). Effective photocatalytic degradation of Congo red dye using alginate/carboxymethyl cellulose/TiO2 nanocomposite hydrogel under direct sunlight irradiation. *Journal of Photochemistry and Photobiology A: Chemistry*, 327, 33-43. DOI: 10.1016/j.jphotochem.2016.05.005

[55] Shaban, M., Ahmed, A.M., Shehata, N., Betiha, M.A., Rabie, M.A. (2020). Ni-doped and Ni/Cr co-doped TiO₂ nanotubes for enhancement of photocatalytic degradation of Methylene blue. *Journal of Colloid and Interface Science*, 555, 31-41. DOI: 10.1016/j.jcis.2019.07.070

[56] Magdalane, C.M., Jothi, A.I., Priyadharsini, G.M.A., Kaviyarasu, K., Simiyon, G.G. (2021). Synthesis and characterization of TiO₂ doped cobalt ferrite nanoparticles via microwave method: Investigation of photocatalytic performance of Congo red degradation dye. *Surfaces and Interfaces*, 25, 1-14. DOI: 10.1016/j.surfin.2021.101296

[57] Zhu, L., Kong, X., Yang, C., Ren, B., Tang, Q. (2020). Fabrication and characterization of the magnetic separation photocatalyst C-TiO₂@Fe₃O₄/AC with enhanced photocatalytic performance under visible light irradiation. *Journal of Hazardous Materials*, 381, 1-14. Doi: 10.1016/j.jhazmat.2019.120910

[58] Namdarian, A, Tabrizi, A.G., Arsalani, N., Khataee, A., Mohammadi, A. (2020). Synthesis of PANi nanoarrays anchored on 2D Bi-OCl nanoplates for photodegradation of Congo red in visible light region. *Journal of Industrial and Engineering Chemistry*, 81, 228-236. DOI: 10.1016/j.jiec.2019.09.012

[59] Shekardasht, M.B., Givianrad, M.H., Gharbani, P., Mirjafary, Z., Mehrizad, A. (2020). Preparation of a novel Z-scheme g-C₃N₄/RGO/Bi₂Fe₄O₉ nanophotocatalyst for degradation of Congo red dye under visible light. *Diamond and Related Materials,* 109, 1-9. DOI: 10.1016/j.diamond.2020.108008

[60] Aboutaleb, W.A., El-Salamony, R.A. (2019). Effect of Fe₂O₃-CeO₂ nanocomposite synthesis method on the Congo red dye photodegradation under visible light irradiation. *Materials Chemistry and Physics*, 236, 1-10. DOI: 10.1016/j.matchemphys.2019.121724

[61] Mandal, S., Adhikari, S., Pu, S., Wang, X., Kim, D., Patel, R.K. (2019). Interactive Fe₂O₃/porous SiO₂ nanospheres for photocatalytic degradation of organic pollutants: kinetic and mechanistic approach. *Chemosphere*, 234, 596-607. DOI: 10.1016/j.chemosphere.2019.06.092

[62] Indira, K., Sathiyavimal, S., Shanmugam, S., Hari, A., Vasantharaj, S., Pugazhendhi, A., Brindhadevi, K., El Askary, A., Elfasakhany, A. (2021). Photocatalytic degradation of Congo red dye using nickel–titanium dioxide nanoflakes synthesized by *Mukia madrasapatna* leaf extract. *Environmental Research*, 202, 1-8. DOI: 10.1016/j.envres.2021.111647

[63] Pourzad, A., Sobhi, H.R., Behbahani, M., Esrafili, A., Kalantary, R.R., Kermani, M. (2020). Efficient visible Light-induced Photocatalytic Removal of Paraquat using N-doped TiO₂@SiO₂@Fe₃O₄ Nanocomposite. *Journal of Molecular Liquids*, 299, 1-7. DOI: 10.1016/j.molliq.2019.112167

[64] Saridewi, N., Komala, S., Zulys, A., Nurbayti, S., Tulhusna, L., Adawiah, A. (2022). Synthesis of ZnO-Fe₃O₄ magnetic nanocomposites through sonochemical methods for Methylene blue degradation. *Bulletin of Chemical Reaction Engineering & Catalysis*, 17(3), 650-660. DOI: 10.9767/bcrec.17.3.15492.650-660

[65] Motlagh, P.Y., Khataee, A., Hassani, A., Orooji, Y. (2023). Facile and environmentally friendly synthesis of highly efficient two-dimensional hematene nanosheets for photocatalytic applications. *Journal of Industrial and Engineering Chemistry*, 1-15. DOI: 10.1016/j.jiec.2023.06.035

[66] Boudiaf, S., Nasrallah, N., Mellal, M., Belhamdi, B., Belabed, C., Djilali, M.A., Trari, M. (2021). Kinetic studies of Congo red photodegradation on the hetero-system CoAl$_2$O$_4$/ZnO with a stirred reactor under solar light. *Journal of Environmental Chemical Engineering*, 9(4), 1-13. DOI: 10.1016/j.jece.2021.105572

[67] Elkodous, M.A., El-Khawaga., A.M., Abouelela, M.M., Maksoud, I.A.A. (2023). Cocatalyst loaded Al-SrTiO$_3$ cubes for Congo red dye photo-degradation under wide range of light. *Scientific Reports*, 13, 1-13. DOI: 10.1038/s41598-023-33249-1

[68] Li, Y., Li, X., Li, J., Yin, J. (2006). Photocatalytic degradation of Methyl orange by TiO$_2$-coated activated carbon and kinetic study. *Water Research*, 40(6), 119-26. DOI: 10.1016/j.watres.2005.12.042

[69] Hamad, H., El-Latif, M.A., Kashyout, A.E., Sadik, W., Feteha, M. (2015). Synthesis and characterization of core/shell/shell magnetic (CoFe$_2$O$_4$/SiO$_2$/TiO$_2$) nanocomposite and TiO$_2$ nanoparticle for photocatalytic activity under UV and visible irradiation. *New Journal of Chemistry*, 39, 3116-3128. DOI: 10.1039/C4NJ01821D

[70] Patra, J.K., Baek, K.H. (2017). Antibacterial activity and synergistic antibacterial potential of biosynthesized silver nanoparticles against foodborne pathogenic bacteria along with its anticandidal and antioxidant effects. *Frontier in Microbiology*, 8, 1-14. DOI: 10.3389/fmicb.2017.00167

[71] Yin, I.X., Zhang, J., Zhao, I.S., Mei, M.L., Li, Q., Chu, C.H. (2020). The antibacterial mechanism of silver nanoparticles and its application in dentistry. *International Journal of Nanomedicine*, 15, 2555-2562. DOI: 10.2147/IJN.S246764

[72] Liao, C., Li, Y., Tjong, S.C. (2019). Bactericidal and cytotoxic properties of silver nanoparticles. *International Journal of Molecular Science*, 20(2), 1-47. DOI: 10.3390/ijms20020449